


Cite this: *RSC Adv.*, 2024, 14, 7081

# Br doping-induced evolution of the electronic band structure in dimorphic and hexagonal SnSe<sub>2</sub> thermoelectric materials†

Se-Jun Kim,<sup>‡a</sup> Minsu Heo,<sup>‡a</sup> Sang-il Kim,<sup>ID</sup> <sup>‡a</sup> Hyunjin Park,<sup>a</sup> Jeong-Yeon Kim,<sup>a</sup> Won-Seon Seo<sup>b</sup> and Hyun-Sik Kim<sup>ID</sup> <sup>\*a</sup>

SnSe<sub>2</sub> with its layered structure is a promising thermoelectric material with intrinsically low lattice thermal conductivity. However, its poor electronic transport properties have motivated extensive doping studies. Br doping effectively improves the power factor and converts the dimorphic SnSe<sub>2</sub> to a fully hexagonal structure. To understand the mechanisms underlying the power factor improvement of Br-doped SnSe<sub>2</sub>, the electronic band parameters of Br-doped dimorphic and hexagonal SnSe<sub>2</sub> should be evaluated separately. Using the single parabolic band model, we estimate the intrinsic mobility and effective mass of the Br-doped dimorphic and hexagonal SnSe<sub>2</sub>. While Br doping significantly improves the mobility of dimorphic SnSe<sub>2</sub> (with the dominant hexagonal phase), it results in a combination of band convergence and band flattening in fully hexagonal SnSe<sub>2</sub>. Br-doped dimorphic SnSe<sub>2</sub> is predicted to exhibit higher thermoelectric performance ( $zT \sim 0.23$  at 300 K) than Br-doped fully hexagonal SnSe<sub>2</sub> ( $zT \sim 0.19$  at 300 K). Characterisation of the other, currently unidentified, structural phases of dimorphic SnSe<sub>2</sub> will enable us to tailor the thermoelectric properties of Br-doped SnSe<sub>2</sub>.

Received 13th November 2023

Accepted 11th February 2024

DOI: 10.1039/d3ra07751a

rsc.li/rsc-advances

Global warming is disrupting ecosystems and reducing biodiversity, which is threatening food production and human well-being.<sup>1,2</sup> The emission of greenhouse gases, such as carbon dioxide (CO<sub>2</sub>), is a major cause of global warming. Fossil fuels, such as coal, oil, and natural gas, are the main source of CO<sub>2</sub> emissions. The burning of these fuels releases CO<sub>2</sub> into the atmosphere, where it traps heat and contributes to climate change.<sup>3</sup> Renewable and sustainable power generation technologies, such as solar, wind, and hydropower, offer a way to reduce CO<sub>2</sub> emissions and combat global warming. These technologies do not produce greenhouse gases, and they can be used to generate electricity, heat homes and businesses, and power transportation.<sup>4</sup> Among these renewable and sustainable power generation technologies, thermoelectric power generation technology is the only technology that can directly generate electricity from waste heat.<sup>5</sup> The efficiency of thermoelectric devices is a key factor in their ability to convert waste heat into electrical energy. The higher the efficiency, the more electrical energy can be produced from the same amount of waste heat.<sup>6</sup> To improve the efficiency of a thermoelectric power generation

device, the performance of the thermoelectric materials used in the device should be increased. The thermoelectric performance of the material is defined with a dimensionless figure-of-merit,  $zT$ . The  $zT$  is expressed by the following eqn (1)

$$zT = \frac{S^2 \sigma T}{\kappa_e + \kappa_l} \quad (1)$$

where  $S$ ,  $\sigma$ ,  $T$ ,  $\kappa_e$ , and  $\kappa_l$  are the Seebeck coefficient, electrical conductivity, absolute temperature, electronic thermal conductivity, and the lattice thermal conductivity, respectively.<sup>7–10</sup> As evident from eqn (1), to achieve a high  $zT$ , it is essential to increase the power factor (PF), which is the product of the  $S$  and the  $\sigma$ , and simultaneously lower the  $\kappa_l$  (the  $\kappa_e$  is linked to the  $\sigma$ ). Unfortunately, the  $S$  and  $\sigma$  are in a trade-off relationship. This means that it is difficult to improve both  $S$  and  $\sigma$  at the same time.<sup>11</sup> However, there are ways to increase the  $zT$  despite the coupled relationship between the  $S$ ,  $\sigma$ , and  $\kappa_e$ . One strategy is to increase PF *via* band engineering (band convergence and resonant states formation), which overcomes the trade-off relationship between the  $S$  and  $\sigma$ .<sup>12–15</sup> Another strategy is to reduce  $\kappa_l$  that is independent of other parameters in  $zT$  *via* defect engineering.<sup>16–18</sup>

Among the various thermoelectric materials, SnSe<sub>2</sub> has received much attention because it has an intrinsically low  $\kappa_l$  due to its layered structure.<sup>19</sup> The layered structure has a distinct difference between the bonding forces within layers and between layers. The bonds within the layer are covalent bonds, which are strong chemical bonds. The bonds between

<sup>a</sup>Department of Materials Science and Engineering, University of Seoul, Seoul 02504, South Korea. E-mail: hyunsik.kim@uos.ac.kr

<sup>b</sup>Department of Materials Science and Engineering, Yonsei University, Seoul 03722, South Korea

† Electronic supplementary information (ESI) available. See DOI: <https://doi.org/10.1039/d3ra07751a>

‡ These authors contributed equally to this study.



layers are van der Waals bonds, which are weaker secondary bonds. As a result, the  $\kappa_1$  along the axis of van der Waals bonding is low, which contributes to lowering  $\kappa_1$ .<sup>20–22</sup> However, pristine SnSe<sub>2</sub> has a low PF due to low  $\sigma$ .<sup>8</sup> Wu *et al.* significantly increased Hall carrier concentration ( $n_H$ ) and Hall mobility ( $\mu_H$ ) compared to the pristine SnSe<sub>2</sub> by Cl doping (12 mol%) at the Se sites. Consequently, the PF is significantly improved (0.0175 → 1.05 mW m<sup>−1</sup> K<sup>−2</sup>) compared to pristine SnSe<sub>2</sub> near room temperature.<sup>23</sup> Wang *et al.* fabricated Cu-doped SnSe<sub>2</sub>, which resulted in a lower  $S$  compared to pristine SnSe<sub>2</sub>, but a higher PF (1.96 mW m<sup>−1</sup> K<sup>−2</sup>) at 300 K due to an increase in  $n_H$ .<sup>24</sup> Li *et al.* achieved a high PF (0.35 mW m<sup>−1</sup> K<sup>−2</sup>) by doping Ag at the Sn sites (1 mol%). The PF increase owing to the Ag doping could be attributed to the  $S$  improvement that outweighed the  $\sigma$  decrease. Although Ag doping improved the  $\mu_H$ , it decreased the  $n_H$  to an extent that the  $\sigma$  decreased with Ag doping.<sup>25</sup> Zhou *et al.* improved the PF (1.2 mW m<sup>−1</sup> K<sup>−2</sup>) of SnSe<sub>2</sub> by co-doping Cu (between the layers of SnSe<sub>2</sub>) and Br (within the layers). The co-doping improved the  $\sigma$  by increasing the  $n_H$  and  $\mu_H$  at the same time.<sup>22</sup> Recently, Liu *et al.* reported that Br doping at Se sites (SnSe<sub>2−x</sub>Br<sub>x</sub> for  $x = 0, 0.01, 0.03, 0.05$ , and  $0.10$ ) was effective in improving the PF.<sup>26</sup> They confirmed that both the  $n_H$  and  $\mu_H$  increased (hence the  $\sigma$  increased) as the Br doping content increased up to  $x = 0.05$ . SnSe<sub>2</sub> has a dimorphic structure, meaning that it can exist in two different crystal structures: hexagonal and unidentified structure.<sup>29–31</sup> These two structures can coexist stably. Liu *et al.*<sup>26</sup> found that the fraction of the hexagonal structure in SnSe<sub>2</sub> increased for the Br doping content ( $x$ ) smaller than 0.05 (although the hexagonal structure is already dominant). However, only the hexagonal structure was detected for  $x \geq 0.05$ . In other words, the Br doping promoted the fraction of the hexagonal structure and increased the  $n_H$  for  $x < 0.05$ , while it only increased the  $n_H$  for  $x \geq 0.05$ . However, how the fraction of hexagonal structure increase (induced by the Br doping) and the Br doping (when SnSe<sub>2</sub> is fully hexagonal) affect the electronic band structure of SnSe<sub>2</sub> is not studied.

In this study, changes in the electronic band structure of SnSe<sub>2</sub> were investigated using the Single Parabolic Band (SPB) model both when Br doping increased the fraction of the hexagonal phase (SnSe<sub>2−x</sub>Br<sub>x</sub> for  $x < 0.05$ ) and when it only increased the  $n_H$  as the SnSe<sub>2−x</sub>Br<sub>x</sub> was fully hexagonal ( $x \geq 0.05$ ). The increase of the hexagonal phase improved the PF of the SnSe<sub>2−x</sub>Br<sub>x</sub> ( $x < 0.05$ ) due to a significant increase in the non-degenerate mobility ( $\mu_0$ ). The increase in the Br doping concentration ( $x$ ) for  $x > 0.05$  also improved the PF but this time by increasing the density-of-states effective mass ( $m_d^*$ ). The theoretical maximum PF of 1.27 mW m<sup>−1</sup> K<sup>−2</sup> was predicted when  $x = 0.03$  (when the SnSe<sub>2−x</sub>Br<sub>x</sub> is not yet in full hexagonal phase) at room temperature. An additional 12% increase in 300 K  $zT$  (0.21 → 0.23) of SnSe<sub>1.7</sub>Br<sub>0.3</sub> ( $x = 0.03$ ) was expected once the  $n_H$  was optimally tuned as the SPB model guided. Understanding the effects of Br doping on the electronic band structure of SnSe<sub>2</sub>, which changes with doping concentration, would enable the development of SnSe<sub>2</sub> materials with tailored thermoelectric properties.

## Single parabolic band model calculation

Electronic band parameters such as  $m_d^*$ ,  $\mu_0$ , weighted mobility ( $\mu_w$ ), and  $B$ -factor were calculated using the SPB model while assuming that only one parabolic band contributed to the electronic transport properties and that the acoustic phonon scattering mechanism was the dominant charge scattering mechanism. The purpose of employing the SPB model here is to guide the improvement of  $zT$ . Because most of the parameters in  $zT$  vary with  $n_H$ , the optimization of the  $n_H$  is essential for the  $zT$  increase. While the vast compositional space of promising thermoelectric materials offers immense potential, efficient optimization transcends solely experimental methods. While computationally intensive methods exist, for experimentalists, simplified Boltzmann transport equation-derived models often provide a pragmatic route to understand thermoelectric material properties. The SPB model, relying on a single parabolic band and effective mass, stands out for its simplicity and effectiveness. Notably, it enables complete characterization of the system using a minimal set of experimentally obtainable quantities ( $S$ ,  $\sigma$ ,  $\kappa$ , and  $n_H$ ), demonstrating its practical utility and simplicity.

### Estimation of density-of-states effective mass, $m_d^*$

Based on the experimental temperature-dependent  $S$  and 300 K  $n_H$  from Liu *et al.*,<sup>26</sup>  $n_H$ -dependent  $S$  at 300 K was obtained. The  $m_d^*$  corresponding to the 300 K  $n_H$ -dependent  $S$  measurement was then acquired by fitting the theoretical  $n_H$ -dependent  $S$  constructed from the following eqn (2)–(4) to the  $n_H$ -dependent  $S$  measurement.

$$S = \frac{k_B}{e} \left( \eta - \frac{2F_1(\eta)}{F_0(\eta)} \right) \quad (2)$$

$$F_j(\eta) = \int_0^\infty \frac{\epsilon^j}{1 + \exp(\epsilon - \eta)} d\epsilon \quad (3)$$

$$n_H = \frac{16\pi}{3} \left( \frac{2m_d^*k_B T}{h^2} \right)^{3/2} \frac{(F_0(\eta))^2}{F_{-0.5}(\eta)} \quad (4)$$

where  $k_B$ ,  $e$ ,  $\eta$ ,  $F_j$ , and  $h$  are the Boltzmann constant, electron charge, reduced chemical potential, fermi integral order of  $j$ , and Planck's constant, respectively. According to eqn (2)–(4) while the  $S$  is only a function of  $\eta$ , the  $n_H$  varies with both  $\eta$  and  $m_d^*$ . We changed  $\eta$  from  $-20$  to  $20$  with a fitted  $m_d^*$  to calculate a theoretical Seebeck pisarenko curve ( $S$  vs.  $n_H$ ) that agreed with the experimental  $n_H$ -dependent  $S$ .<sup>26</sup>

### Estimation of non-degenerate mobility, $\mu_0$

We computed theoretical  $n_H$ -dependent Hall mobility ( $\mu_H$ ) using eqn (4) and (5).<sup>27</sup>

$$\mu_H = \mu_0 \frac{F_{-0.5}(\eta)}{2F_0(\eta)} \quad (5)$$



The  $\mu_0$  included in  $\mu_H$  (eqn (5)) was fitted so that the theoretical  $n_H$ -dependent  $\mu_H$  agreed with the experimental  $n_H$ -dependent  $\mu_H$ . When the  $n_H$  was calculated to construct the theoretical  $n_H$ -dependent  $\mu_H$ , the same  $m_d^*$  fitted to construct the  $n_H$ -dependent  $S$  of the same sample was adopted.

### Estimation of weighted mobility, $\mu_w$ , and $B$ -factor, $B$

Once we have obtained the  $m_d^*$  and  $\mu_0$  of the  $\text{SnSe}_{2-x}\text{Br}_x$  samples, corresponding  $\mu_w$  and  $B$ -factor were calculated using the following eqn (6) and (7), respectively.<sup>32–34</sup> In eqn (6) and (7), the  $m_e$  is the electron rest mass.

$$\mu_w = \mu_0 \left( \frac{m_d^*}{m_e} \right)^{3/2} \quad (6)$$

$$B = \left( \frac{k_B}{e} \right)^2 \frac{8\pi e (2m_e k_B)^{3/2}}{h^3} \frac{\mu_w T^{5/2}}{\kappa_1} \quad (7)$$

## Results and discussion

Fig. 1(a) shows the experimental and calculated  $n_H$ -dependent  $S$  of  $\text{SnSe}_{2-x}\text{Br}_x$  samples ( $x = 0, 0.01, 0.03, 0.05, 0.1$ ) at 300 K. The symbols represent those measurements reported by Liu *et al.*<sup>26</sup>

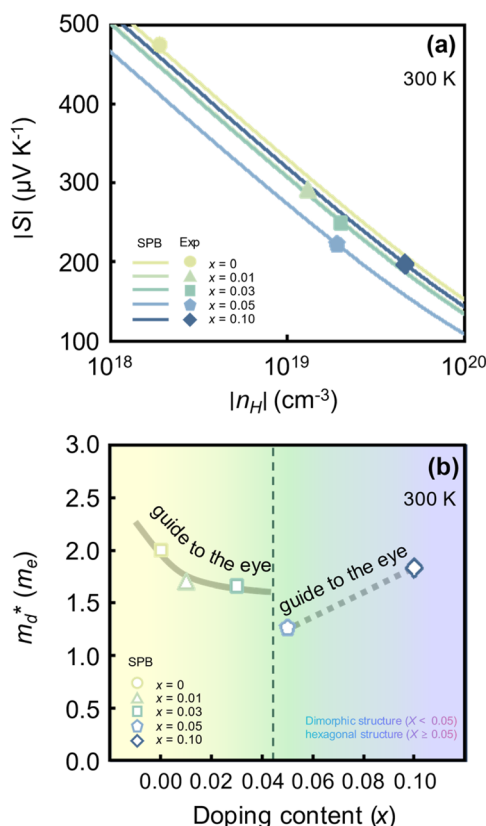


Fig. 1 (a) Experimental (symbols) and theoretical (lines) Hall carrier concentration ( $n_H$ )-dependent Seebeck coefficient ( $S$ ) of  $\text{SnSe}_{2-x}\text{Br}_x$  ( $x = 0-0.10$ ) at 300 K.<sup>26</sup> (b) Density-of-states effective mass ( $m_d^*$ ) as a function of Br doping content ( $x$ ) at 300 K.

(refer to Fig. S1(a) in ESI† for temperature-dependent  $S$  of  $\text{SnSe}_{2-x}\text{Br}_x$  at higher temperatures). The lines represent theoretical  $S$  as a function of  $n_H$  for different  $x$  computed by using the SPB model. The experimental  $S$  (in symbols) decreases as  $x$  increases. The rate of  $S$  decrease is particularly high when  $x$  is low. For example, the experimental  $S$  of pristine  $\text{SnSe}_2$  ( $x = 0$ ) decreases by more than 39% when  $x$  increases to 0.01 ( $475 \rightarrow 289 \mu\text{V K}^{-1}$ ). In contrast, the experimental  $n_H$  generally increases as  $x$  increases. For example, the  $n_H$  of the  $x = 0.1$  sample ( $4.6 \times 10^{19} \text{ cm}^{-3}$ ) is higher than that of the pristine sample ( $0.19 \times 10^{19} \text{ cm}^{-3}$ ) by more than a factor of 24. However, when  $x$  increases from 0.03 to 0.05, we observe a slight drop in  $n_H$  from  $2.0 \times 10^{19}$  to  $1.9 \times 10^{19} \text{ cm}^{-3}$ . The  $x$  increase increases the fraction of the hexagonal phase within the sample only for  $x < 0.05$ . Because the  $\text{SnSe}_{2-x}\text{Br}_x$  samples with  $x \geq 0.05$  is fully hexagonal, the effect of Br doping would be different from that observed at  $x < 0.05$ . It is when the sample becomes fully hexagonal ( $x = 0.05$ ) that we observe an exception in the general trend of increasing  $n_H$  with an increasing  $x$ . The calculated  $n_H$ -dependent  $S$  obtained by fitting  $m_d^*$  (in lines) are all in agreement with the symbol data. This implies that the fitted  $m_d^*$  accurately reflects the electronic band structure of the  $\text{SnSe}_{2-x}\text{Br}_x$  samples.

Fig. 1(b) shows the  $x$ -dependent  $m_d^*$  fitted using the SPB model at 300 K. Fig. 1(b) is divided into two regions: yellow and purple regions. The yellow region is when the  $\text{SnSe}_{2-x}\text{Br}_x$  samples exist as a dimorphic phase (hexagonal structure + unidentified structure). As the  $x$  increases from 0 to 0.05, the fraction of the hexagonal phase increases. At  $x = 0.05$ , the  $\text{SnSe}_{2-x}\text{Br}_x$  becomes fully hexagonal. The color of the background also changes from yellow to purple at  $x = 0.05$ , which means that the dimorphic structure transforms to the full hexagonal structure. For  $x \geq 0.05$ , the samples are all hexagonal. So this region is colored in purple. The  $m_d^*$  decreases from the pristine sample to  $x = 0.05$  sample. For example, the  $m_d^*$  of pristine and  $x = 0.05$  sample are  $2.00 m_e$  and  $1.26 m_e$ , respectively. This 37% decrease in  $m_d^*$  is closely related to the dimorphic structure changing to fully hexagonal phase. Once the Br doping finishes stabilizing the hexagonal phase, further Br doping starts to increase the  $m_d^*$  again. The  $m_d^*$  of the  $x = 0.1$  sample increase to  $1.83 m_e$ , which is approximately 45% heavier than that of  $x = 0.05$  sample. The  $m_d^*$  increase at  $x > 0.05$  may be related to the band convergence. According to Kim *et al.*,<sup>34</sup> there exists another conduction band near (in energy) the major conduction band in the calculated band structure of  $\text{SnSe}_2$ . However, the change in  $\mu_0$  with increasing  $x$  also needs to be evaluated to confirm a possible band convergence at  $x > 0.5$ . Our  $m_d^*$  for  $\text{SnSe}_{2-x}\text{Br}_x$  determined by the SPB model spans a range of  $\sim 1.0$  to  $2.0 m_e$ , aligning with values reported in previous studies also using the SPB model.<sup>35</sup>

Fig. 2(a) shows the experimental and calculated  $n_H$ -dependent  $\mu_H$  at 300 K. The symbols represent the experimental  $n_H$ -dependent  $\mu_H$  of  $\text{SnSe}_{2-x}\text{Br}_x$  ( $x = 0, 0.01, 0.03, 0.05, 0.1$ ) at 300 K reported by Liu *et al.*<sup>26</sup> (refer to Fig. S1(b)† for temperature-dependent  $\sigma$  of  $\text{SnSe}_{2-x}\text{Br}_x$  at higher temperatures). The lines represent the  $n_H$ -dependent  $\mu_H$  calculated using the SPB model. The experimental  $\mu_H$  initially increases as the  $x$  increases from



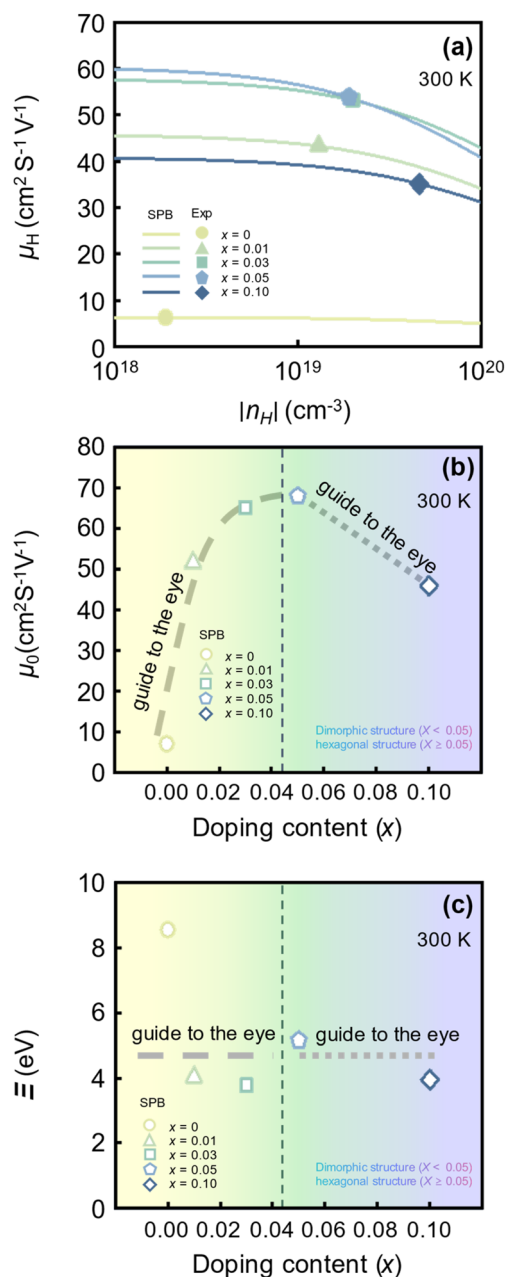


Fig. 2 (a) Experimental (symbols) and theoretical (lines) Hall carrier concentration ( $n_H$ )-dependent hall mobility ( $\mu_H$ ) of  $\text{SnSe}_{2-x}\text{Br}_x$  ( $x = 0-0.1$ ) at 300 K.<sup>26</sup> (b) Non-degenerate mobility ( $\mu_0$ ) and (c) deformation potential ( $\Xi$ ) as a function of Br doping content ( $x$ ) at 300 K.

0 to 0.03. The amount of  $\mu_H$  increase rapidly decreases as  $x$  approaches 0.03. When the  $x$  increases from 0.03 to 0.05, the change in  $\mu_H$  is almost negligible. However, as  $x$  further increases to 0.1, the corresponding  $\mu_H$  decreases significantly. The  $\mu_H$  of the  $x = 0.05$  sample ( $53.9 \text{ cm}^2 \text{ V}^{-1} \text{ s}^{-1}$ ) is approximately 8 times higher than that of the pristine sample ( $6.3 \text{ cm}^2 \text{ V}^{-1} \text{ s}^{-1}$ ). However, the  $\mu_H$  of the  $x = 0.1$  sample is 35% lower than that of the  $x = 0.05$  sample. As the fraction of hexagonal structures occupying dimorphic structures increases up to  $x =$

0.05, the corresponding  $\mu_H$  increases. However, once the hexagonal structure is stabilized Br doping decreases the  $\mu_H$ .

Fig. 2(b) shows the  $x$ -dependent  $\mu_0$  calculated using the SPB model. The  $\mu_0$  as a function of  $x$  resembles an inverted U-shape. As the fraction of the hexagonal phase increases the  $\mu_0$  saturates to  $68.0 \text{ cm}^2 \text{ V}^{-1} \text{ s}^{-1}$  at  $x = 0.05$ . It is to be noted that the slight increase in hexagonal phase fraction significantly improves the  $\mu_0$ . For  $x \geq 0.05$ , as the Br doping content increases in the fully hexagonal  $\text{SnSe}_{2-x}\text{Br}_x$  samples, the  $\mu_0$  rapidly decreases back to  $46.0 \text{ cm}^2 \text{ V}^{-1} \text{ s}^{-1}$  ( $x = 0.1$ ). This is exactly the opposite of the trend observed in  $x$ -dependent  $m_d^*$  (Fig. 1(b)). If the change in  $\mu_0$  with an increasing  $x$  for  $x \geq 0.05$  is negligible, we could have concluded that the  $m_d^*$  increase for  $x \geq 0.05$  is due to band convergence. On the contrary, the  $m_d^*$  increase accompanied by a decrease in  $\mu_0$  can be characterized by a simple band flattening which is not beneficial to the PF improvement. However, while the majority band is being flattened, the neighbouring band may also contribute to the electronic transport due to Br doping. This can be evaluated when the weighted mobility ( $\mu_w$ ) is calculated.

Fig. 2(c) shows the  $x$ -dependent deformation potential ( $\Xi$ ) calculated by the SPB model. The  $\Xi$  is closely related to the  $\mu_0$  as defined in eqn (8).

$$\mu_0 = \left( \frac{e\pi\hbar^4 C_1}{\sqrt{2}\Xi^2 (k_B T)^{3/2}} \right) \left( \frac{1}{m_b^*} \right)^{5/2} \quad (8)$$

where the  $C_1$  and  $m_b^*$  are the elastic constant and the single band mass, respectively. The  $m_b^*$  is coupled to  $m_d^*$  as shown below.

$$m_d^* = N_V^{2/3} m_b^* \quad (9)$$

The product between  $N_V^{2/3}$  and  $m_b^*$ , where  $N_V$  is the valley degeneracy, defines the  $m_d^*$ . When the  $m_d^*$  increase is driven by the  $N_V$  increase (no change in  $m_b^*$ ), the band convergence occurs.<sup>13,28</sup> However, when  $m_d^*$  increase is driven by the  $m_b^*$  increase (no change in  $N_V$ ), a band flattening occurs. For this reason, the nature of  $m_d^*$  increase needs to be evaluated by the corresponding change in  $\mu_0$ . Unlike  $\mu_0$ , the  $\Xi$  is independent of  $m_d^*$  and captures the strength of the carrier-phonon interaction. According to Fig. 2(c), Br doping in  $\text{SnSe}_2$  decreases the  $\Xi$ , but varying Br doping content ( $x$ ) does not have a strong impact on the  $\Xi$ . For example, the  $\Xi$  of  $\text{SnTe}$  decreased by more than 55% when it is doped with  $x = 0.01$  Br ( $8.56 \rightarrow 3.79 \text{ eV}$ ). However, it remained relatively constant for increasing  $x$ . In other words, neither changing the hexagonal phase ( $x < 0.05$ ) nor increasing the Br doping content in a stabilized hexagonal phase ( $x \geq 0.05$ ) has a significant impact on how phonons scatter charged carriers.

Fig. 3(a) shows the  $x$ -dependent  $\mu_w$  of  $\text{SnSe}_{2-x}\text{Br}_x$  ( $x = 0.0-0.10$ ) calculated by using the SPB model at 300 K. The  $\mu_w$ , which is defined as the product of  $\mu_0$  and  $(m_d^*/m_e)^{3/2}$  (as presented in eqn (6)), captures the potential of a material achieve a high PF, as it depends on both the  $\mu_0$  and the  $m_d^*$ . Compared to the pristine  $\text{SnSe}_2$  sample ( $x = 0.0$ ), the Br-doped  $\text{SnSe}_2$  samples ( $x > 0.0$ ) have a significantly higher  $\mu_w$ . When Br doping increases the fraction of the hexagonal phase ( $x < 0.05$ ), the  $\mu_w$  increases





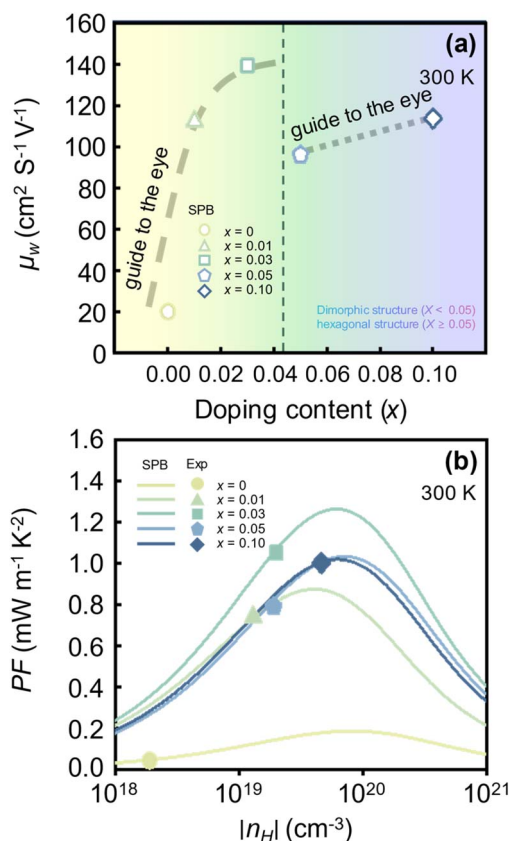


Fig. 3 (a) Calculated weighted mobility ( $\mu_w$ ) of  $\text{SnSe}_{2-x}\text{Br}_x$  ( $x = 0.0-0.10$ ) estimated with varying Br doping content ( $x$ ) at 300 K. (b) Calculated and experimental Hall carrier concentration ( $n_H$ )-dependent power factor (PF) of  $\text{SnSe}_{2-x}\text{Br}_x$  ( $x = 0.0-0.10$ ) at 300 K.<sup>26</sup>

significantly (guide-to-the-eye in grey line). For example, the  $\mu_w$  of the pristine sample ( $x = 0.0$ ) and the  $x = 0.03$  sample are 20.22 and  $139.39 \text{ cm}^2 \text{V}^{-1} \text{s}^{-1}$ , respectively, which is a 5.8-fold increase. Additional Br doping on stabilized hexagonal phase ( $x \geq 0.05$ ) also improves the  $\mu_w$  (guide-to-the-eye in grey line). Although the  $\mu_w$  increase is observed for both  $x < 0.05$  and  $x \geq 0.05$  regions with increasing  $x$ , the reason behind the  $\mu_w$  improvement differs. When  $x < 0.05$ , the  $\mu_w$  increase with  $x$  is due to the  $\mu_0$  increase (Fig. 2(b)), but when  $x \geq 0.05$ , the  $\mu_w$  increase can be attributed to the  $m_d^*$  increase (Fig. 1(b)). The increase in  $m_d^*$  with increasing  $x$  at  $x \geq 0.05$  is due to both band flattening and band convergence. Specifically, the lowest conduction band that contributes majorly to electronic transports becomes heavier, while the second lowest conduction band approaches the lowest conduction band in energy as Br is doped into the fully hexagonal  $\text{SnSe}_2$ . Evidence for band flattening and band convergence is provided by the decrease in  $\mu_0$  (Fig. 2(b)) and the increase in  $\mu_w$  (Fig. 3(a)) at  $x \geq 0.05$ , respectively. The discontinuity in the  $\mu_w$  when  $x$  increases from 0.03 to 0.05 is due to a sudden drop in the  $m_d^*$  of the fully hexagonal phase  $x = 0.05$  sample (Fig. 1(b)). Although the unidentified phase comprises a small fraction of the  $x = 0.03$  sample, its conversion to hexagonal phase is responsible for the decrease in  $m_d^*$ .

Fig. 3(b) shows the PF as a function of the  $n_H$ . The experimentally measured PF reported by Liu *et al.*<sup>26</sup> is represented by the symbols, while the theoretically calculated PF is represented by the lines. Experimentally, Br doping improves the PF in both  $x < 0.05$  and  $x \geq 0.05$  regions. When  $x < 0.05$ , the PF of the  $x = 0.03$  sample ( $1.05 \text{ mW m}^{-1} \text{K}^{-2}$ ) is approximately 25 times higher than that of the pristine  $\text{SnSe}_2$  sample ( $0.04 \text{ mW m}^{-1} \text{K}^{-2}$ ). For  $x \geq 0.05$ , the PF of the  $x = 0.10$  sample ( $1.00 \text{ mW m}^{-1} \text{K}^{-2}$ ) is 27% higher than that of the  $x = 0.05$  sample ( $0.79 \text{ mW m}^{-1} \text{K}^{-2}$ ). From the  $x$ -dependent  $\mu_w$  (Fig. 3(a)), we found that both band flattening and band convergence are present in the  $x = 0.10$  sample. However, the theoretical maximum PF of the  $x = 0.10$  sample ( $1.02 \text{ mW m}^{-1} \text{K}^{-2}$ ) is not as high as that of the  $x = 0.03$  sample ( $1.27 \text{ mW m}^{-1} \text{K}^{-2}$ ). According to the SPB model, the PF of the  $x = 0.03$  sample can be enhanced by more than 21% with an appropriate optimization of the  $n_H$  ( $1.05 \rightarrow 1.27 \text{ mW m}^{-1} \text{K}^{-2}$ ). The theoretical maximum PF and its corresponding  $n_H$  predicted by the SPB model exhibit reasonable agreement with those obtained from Density Functional Theory (DFT) calculations. For example, the SPB model predicts a peak PF of  $0.17 \text{ mW m}^{-1} \text{K}^{-2}$  for pristine  $\text{SnSe}_2$  ( $x = 0$ ) at  $n_H = 8 \times 10^{19} \text{ cm}^{-3}$  (Fig. 3(b)), while DFT calculations yield a peak PF of  $0.13 \text{ mW m}^{-1} \text{K}^{-2}$  at  $n = 5 \times 10^{19} \text{ cm}^{-3}$ .<sup>36</sup> It is important to note that the maximum PF is predicted to occur before the sample is fully hexagonal.

Fig. 4(a) shows the  $x$ -dependent  $B$ -factor of  $\text{SnSe}_{2-x}\text{Br}_x$  ( $x = 0.0-0.10$ ) at 300 K calculated by the SPB model. The  $B$ -factor, which is proportional to the ratio of  $\mu_0$  to  $\kappa_1$ , is related to the theoretically achievable  $zT$  (eqn (7)). The trend observed in the  $B$ -factor is similar to that observed in the  $\mu_0$ , as shown in Fig. 3(a). This is possible because the  $\kappa_1$  of the Br-doped  $\text{SnSe}_2$  decreases linearly with increasing  $x$  (Fig. 4(b)). When Br was first doped into  $\text{SnSe}_2$  with  $x = 0.01$ , its  $\kappa_1$  increased by 11% compared to the pristine  $\text{SnSe}_2$  ( $1.34 \rightarrow 1.48 \text{ W m}^{-1} \text{K}^{-1}$ ). However, when  $x$  was increased further, the  $\kappa_1$  decreased gradually. Both increasing the hexagonal phase fraction ( $0 < x < 0.05$ ) and increasing the Br doping in the full hexagonal phase ( $x \geq 0.05$ ) reduced the  $\kappa_1$  (refer to Fig. S1(c)† for temperature-dependent total thermal conductivity ( $\kappa_{\text{tot}}$ ) of  $\text{SnSe}_{2-x}\text{Br}_x$  at higher temperatures). The calculated Lorenz number ( $L$ ) and  $\kappa_e$  used to estimate  $\kappa_1$  are provided in Fig. S2.† Initial increase in the  $\kappa_1$  of the  $x = 0.01$  sample requires further study. While an initial increase in  $\kappa_1$  upon Br doping of  $\text{SnSe}_2$  has been reported previously,<sup>37</sup> similar observations in Cl-doped  $\text{SnSe}_2$  suggest a broader phenomenon beyond specific dopant species.<sup>38</sup> Elucidating the underlying mechanism governing this low-concentration dopant-induced thermal conductivity enhancement warrants further investigation. The effect of decreasing the unidentified phase on the  $B$ -factor is stronger than that of increasing the Br doping content in the fully hexagonal phase. Although the  $B$ -factor improved by a factor of 6 when pristine  $\text{SnSe}_2$  was doped with  $x = 0.03$  ( $0.01 \rightarrow 0.06$ ), once  $\text{SnSe}_2$  was fully hexagonal, additional Br doping only improved the  $B$ -factor by 25% as  $x$  increased from 0.05 to 0.10 ( $0.04 \rightarrow 0.05$ ). However, if the  $x$  is increased beyond 0.10, the  $B$ -factor of the sample may become higher than that of the  $x = 0.03$  sample due

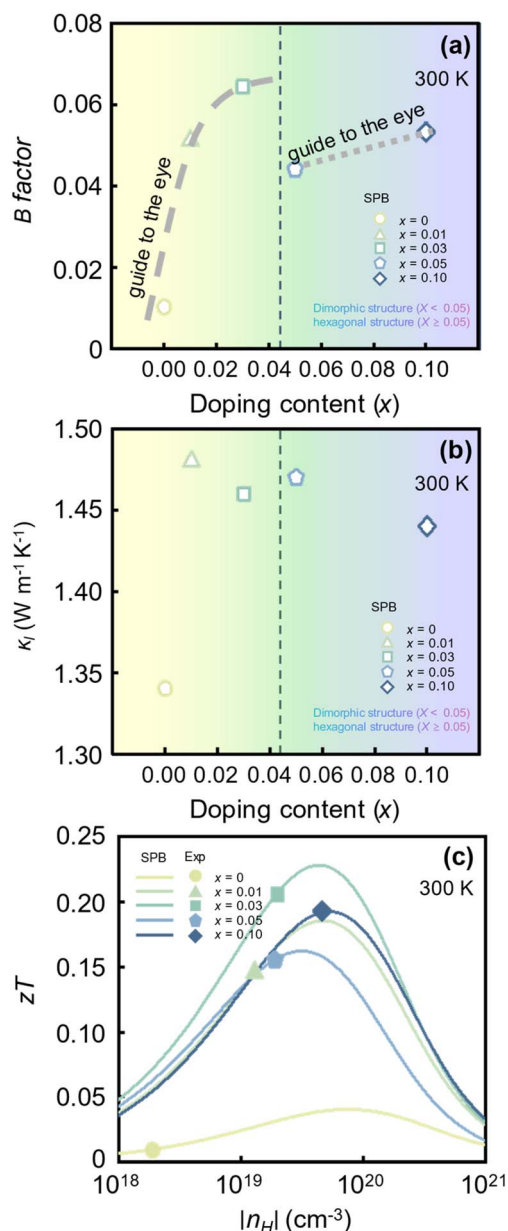


Fig. 4 Calculated (a)  $B$ -factor and (b) lattice thermal conductivity ( $\kappa_l$ ) of  $\text{SnSe}_{2-x}\text{Br}_x$  ( $x = 0.0$ – $0.10$ ) at 300 K. (c) Calculated and experimental<sup>27</sup>  $zT$  of  $\text{SnSe}_{2-x}\text{Br}_x$  ( $x = 0.0$ – $0.10$ ) with varying Hall carrier concentration ( $n_H$ ).

to the combined effects of band convergence and  $\kappa_l$  reduction becoming stronger.

Fig. 4(c) shows experimental and calculated  $n_H$ -dependent  $zT$  at 300 K (refer to Fig. S1(d)† for temperature-dependent  $zT$  of  $\text{SnSe}_{2-x}\text{Br}_x$  at higher temperatures). The symbols represent the measured values.<sup>26</sup> The lines represent  $zT$  computed by the SPB model-based calculation. The calculated maximum  $zT$  of pristine  $\text{SnSe}_2$  is low, as illustrated in Fig. 4(c). Temperature-dependent  $zT$  calculations for pristine  $\text{SnSe}_2$  below 300 K are presented in Fig. S1 (ESI†), revealing a maximum at 300 K exceeding those at 50 and 100 K. This finding underscores the pronounced temperature-dependent  $zT$  of  $\text{SnSe}_2$ .<sup>24</sup> However, the

maximum  $zT$  improves drastically as Br is doped into  $\text{SnSe}_2$ . For example, the calculated maximum  $zT$  of pristine  $\text{SnSe}_2$  and  $x = 0.03$  samples are 0.04 and 0.23, respectively, which is an increase of more than 5 times. Once the  $\text{SnSe}_2$  is a fully hexagonal phase ( $x \geq 0.05$ ), additional Br doping is also beneficial to the calculated maximum  $zT$ . The calculated maximum  $zT$  of the  $x = 0.05$  and  $0.10$  samples are 0.16 and 0.19, respectively (19% improvement in  $zT$ ). According to the SPB model calculations, adjusting the  $n_H$  of the  $x = 0.03$  sample to  $3.6 \times 10^{19} \text{ cm}^{-3}$  can improve the  $zT$  to 0.23, an approximately 10% increase compared to the experimental  $zT$ . Furthermore, it is highly likely that further Br doping beyond  $x = 0.10$  may result in even higher  $zT$  because of the interplay between the band convergence and intensified point-defect phonon scattering.

## Conclusions

In summary, the effect of Br doping on the electronic band structure of dimorphic  $\text{SnSe}_2$  ( $\text{SnSe}_{2-x}\text{Br}_x$  for  $x = 0, 0.01, 0.03, 0.05$ , and  $0.10$ ) is investigated using the Single Parabolic Band (SPB) model. For Br doping concentrations ( $x$ )  $< 0.05$ , the fraction of the majority hexagonal phase increases with  $x$ , while the other phase remains unidentified. On the contrary, for  $x \geq 0.05$ , the Br-doped  $\text{SnSe}_2$  is fully hexagonal. For all  $x$ , the Hall carrier concentration ( $n_H$ ) increases with  $x$ . The mechanisms underlying the power factor improvement of Br-doped  $\text{SnSe}_2$  with increasing  $n_H$  differ depending on the  $x$ . For  $x < 0.05$ , the increasing hexagonal phase significantly improves the mobility, while for the  $x \geq 0.05$ , the power factor is improved by a combination of band convergence and band flattening. The highest power factor is predicted when a small amount of unidentified phase exists in the  $\text{SnSe}_{2-x}\text{Br}_x$  ( $x = 0.03$ ). Characterization of the unidentified phase in the dimorphic  $\text{SnSe}_2$  is to be carried out to tailor the thermoelectric properties of the  $\text{SnSe}_2$ .

## Author contributions

Se-Jun Kim: conceptualization, investigation, writing – original draft. Minsu Heo: investigation, software, writing – original Draft. Sang-il Kim: validation, methodology, writing – original draft. Hyunjin Park: data curation. Jeong-Yeon Kim: visualization. Won-Seon Seo: validation. Hyun-Sik Kim: supervision, funding acquisition, writing – review & editing.

## Conflicts of interest

There are no conflicts to declare.

## Acknowledgements

This work was supported by the National Research Foundation of Korea (NRF) grant funded by the Korea government (MSIT) (RS-2023-00212959). This research was also supported by Basic Science Research Program through the National Research Foundation of Korea (NRF) funded by the Ministry of Education (NRF-2019R1A6A1A11055660).



## Notes and references

- 1 T. Wu, L. Xia, M. Zhuang, J. Pan, J. Liu, W. Dai, Z. Zhao, M. Zhang, X. Shen, P. He, J. Zhang and Y. Qin, *J. Mar. Sci. Eng.*, 2023, **11**, 9.
- 2 O. Adam, N. Liberty-Levi, M. Byrne and T. Birner, *Geophys. Res. Lett.*, 2022, **50**, e2022GL102546.
- 3 A. A. Khasnis and M. D. Nettleman, *Arch. Med. Res.*, 2005, **36**, 689–696.
- 4 J. Lee, K. A. Lin, S. Jung and E. E. Kwon, *Chem. Eng. J.*, 2023, **452**, 139218.
- 5 S. LeBlanc, *Sustainable Mater. Technol.*, 2014, **1–2**, 26–35.
- 6 P. Fernández-Yáñez, V. Romero, O. Armas and G. Cerretti, *Appl. Therm. Eng.*, 2021, **196**, 117291.
- 7 Y. Zheng, Q. Zhang, X. Su, H. Xie, S. Shu, T. Chen, G. Tan, Y. Yan, X. Tang, C. Uher and G. J. Snyder, *Adv. Energy Mater.*, 2014, **5**, 1401391.
- 8 A. Pham, T. Vu, C. Cheng, T. Trinh, J.-E. Lee, H. Ryu, C. Hwang, S.-K. Mo, J. Kim, L. Zhao, A. Duong and S. Cho, *ACS Appl. Energy Mater.*, 2020, **3**, 10787–10792.
- 9 D. Enescu and E. O. Virjoghe, *Renew. Sust. Energ. Rev.*, 2014, **38**, 903–916.
- 10 C. Zhou, Y. K. Lee, Y. Yu, S. Byun, Z.-Z. Luo, H. Lee, B. Ge, Y.-L. Lee, X. Chen, J. Y. Lee, O. Cojocaru-Mirédin, H. Chang, J. Im, S.-P. Cho, M. Wuttig, V. P. Dravid, M. G. Kanatzidis and I. Chung, *Nat. Mater.*, 2021, **20**, 1378–1384.
- 11 A. Sakai, T. Kanno, K. Takahashi, H. Tamaki, H. Kusada, Y. Yamada and H. Abe, *Sci. Rep.*, 2014, **4**, 6089.
- 12 Y. Pei, H. Wang and G. J. Snyder, *Adv. Mater.*, 2012, **24**, 6125–6135.
- 13 K. H. Lee, S.-i. Kim, H.-S. Kim and S. W. Kim, *ACS Appl. Energy Mater.*, 2020, **3**, 2214–2223.
- 14 S. Ning, S. Huang, Z. Zhang, N. Qi, M. Jiang, Z. Chen and X. Tang, *J. Materiomics*, 2022, **8**, 1086–1094.
- 15 M. Heo, S.-H. Kwon, S.-i. Kim, H. Park, K. H. Lee and H.-S. Kim, *J. Alloys Compd.*, 2023, **954**, 170144.
- 16 Y. Zheng, T. J. Slade, L. Hu, X. Y. Tan, Y. Luo, Z.-Z. Luo, J. Xu, Q. Yan and M. G. Kanatzidis, *Chem. Soc. Rev.*, 2021, **50**, 9022–9054.
- 17 V. Karthikeyan, S. L. Oo, J. U. Surjadi, X. Li, V. C. S. Theja, V. Kannan, S. C. Lau, Y. Lu, K. Lam and V. A. L. Roy, *ACS Appl. Mater. Interfaces*, 2021, **13**, 58701–58711.
- 18 Y. Zhang, Z. Li, S. Singh, A. Nozariasbmarz, W. Li, A. Genç, Y. Xia, L. Zheng, S. H. Lee, S. K. Karan, G. K. Goyal, N. Liu, S. M. Mohan, Z. Mao, A. Cabot, C. Wolverton, B. Poudel and S. Priya, *Adv. Mater.*, 2022, **35**, 2208994.
- 19 Y. Wu, W. Li, A. Faghaninia, Z. Chen, J. Li, X. Zhang, B. Gao, S. Lin, B. Zhou, A. Jain and Y. Pei, *Mater. Today Phys.*, 2017, **3**, 127–136.
- 20 G. Li, G. Ding and G. Gao, *J. Condens. Matter Phys.*, 2016, **29**, 015001.
- 21 S. Bai, M. Wu, J. Zhang, D. Luo, D. Wan, X. Li and S. Tang, *Chem. Eng. J.*, 2023, **455**, 140832.
- 22 C. Zhou, Y. Yu, X. Zhang, Y. Cheng, J. Xu, Y. K. Lee, B. Yoo, O. Cojocaru-Mirédin, G. Liu, S.-P. Cho, M. Wuttig, T. Hyeon and I. Chung, *Adv. Funct. Mater.*, 2019, **30**, 1908405.
- 23 S. Wu, C. Liu, Z. Wu, L. Miao, J. Gao, X. Hu, J. Chen, Y. Zheng, X. Wang, C. Shen, H. Yang and X. Zhou, *Ceram. Int.*, 2019, **45**, 82–89.
- 24 J. Wang, X. Jia, S. Lou, G. Li and S. Zhou, *ACS Omega*, 2020, **5**, 12409.
- 25 F. Li, Z. Zheng, W. Wang, J.-F. Li, B. Li, A. Zhong, J. Luo and P. Fan, *J. Mater. Sci.*, 2017, **52**, 10506–10516.
- 26 M. Liu, J. Zhang, J. Xu, B. Hu, B. Liu, K. Sun, Y. Yang, J. Wang and B. Du, *J. Solid State Chem.*, 2020, **289**, 121468.
- 27 H. Park, S.-i. Kim, J.-Y. Kim, S.-M. Hwang and H.-S. Kim, *Ceramics*, 2023, **6**, 504–513.
- 28 H.-S. Kim, N. A. Heinz, Z. M. Gibbs, Y. Tang, S. D. Kang and G. J. Snyder, *Mater. Today*, 2017, **20**, 452–459.
- 29 V. P. Bhatt, K. Gireesan and G. R. Pandya, *J. Cryst. Growth*, 1989, **96**, 649–651.
- 30 L. Amalraj, M. Jayachandran and C. Sanjeeviraja, *Mater. Res. Bull.*, 2004, **39**, 2193–2201.
- 31 M. Kumar, S. Rani, Y. Singh, K. S. Gour and V. N. Singh, *RSC Adv.*, 2021, **11**, 6477–6503.
- 32 H. Naithani and T. Dasgupta, *ACS Appl. Energy Mater.*, 2020, **3**, 2200–2213.
- 33 M. Kim, S.-i. Kim, S. W. Kim, H.-S. Kim and K. H. Lee, *Adv. Mater.*, 2021, **33**, 2005931.
- 34 S.-i. Kim, J. Bang, J. An, S. Hong, G. Bang, W. H. Shin, T. Kim and K. Lee, *J. Alloys Compd.*, 2021, **868**, 159161.
- 35 Y. Wu, W. Li, A. Faghaninia, Z. Chen, J. Li, X. Zhang, B. Gao, S. Lin, B. Zhou, A. Jain and Y. Pei, *Mater. Today*, 2017, **3**, 127–136.
- 36 D. Sree Sourav, Md. Golam Rosul and M. Zebarjadi, *J. Phys. Chem. C*, 2017, **127**, 6916–6924.
- 37 C. Zhou, Y. Yu, X. Zhang, Y. Cheng, J. Xu, Y. K. Lee, B. Yoo, O. Cojocaru-Mirédin, G. Liu, S.-P. Cho, M. Wuttig, T. Hyeon and I. Chung, *Adv. Funct. Mater.*, 2020, **30**, 1908405.
- 38 S. Wu, C. Liu, Z. Wu, L. Miao, J. Gao, X. Hu, J. Chen, Y. Zheng, X. Wang, C. Shen, H. Yang and X. Zhou, *Ceram. Int.*, 2019, **45**, 82.

